



(This is a sample cover image for this issue. The actual cover is not yet available at this time.)

This article appeared in a journal published by Elsevier. The attached copy is furnished to the author for internal non-commercial research and education use, including for instruction at the authors institution and sharing with colleagues.

Other uses, including reproduction and distribution, or selling or licensing copies, or posting to personal, institutional or third party websites are prohibited.

In most cases authors are permitted to post their version of the article (e.g. in Word or Tex form) to their personal website or institutional repository. Authors requiring further information regarding Elsevier's archiving and manuscript policies are encouraged to visit:

<http://www.elsevier.com/copyright>



The effect of curvature on weathering rind formation: Evidence from Uranium-series isotopes in basaltic andesite weathering clasts in Guadeloupe

Lin Ma^{a,b,c,*}, Francois Chabaux^b, Eric Pelt^b, Mathieu Granet^b, Peter B. Sak^d, Jerome Gaillardet^e, Marina Lebedeva^a, Susan L. Brantley^a

^a Earth and Environmental Systems Institute, Pennsylvania State University, University Park, PA 16802, USA

^b Laboratoire d'Hydrologie et de Géochimie de Strasbourg, EOSt, University of Strasbourg and CNRS, Strasbourg, France

^c Department of Geological Sciences, University of Texas at El Paso, El Paso, TX 79968-0555, USA

^d Department of Earth Sciences, Dickinson College, Carlisle, PA 17013, USA

^e Laboratoire de Géochimie et Cosmochimie, Institut de Physique du Globe de Paris, Paris, France

Received 28 March 2011; accepted in revised form 21 November 2011

Abstract

To quantify rates of rind formation on weathering clasts under tropical and humid climate and to determine factors that control weathering reactions, we analyzed Uranium series isotope compositions and trace element concentrations in a basaltic andesite weathering clast collected from Basse-Terre Island in Guadeloupe. U, Th, and Ti elemental profiles reveal that Th and Ti behave conservatively during rind formation, but that U is added from an external source to the rind. In the rind, weathering reactions include dissolution of primary minerals such as pyroxene, plagioclase, and glass matrix, as well as formation of Fe oxyhydroxides, gibbsite and minor kaolinite. Rare earth element (REE) profiles reveal a significant Eu negative anomaly formed during clast weathering, consistent with plagioclase dissolution. Significant porosity forms in the rind mostly due to plagioclase dissolution. The new porosity is inferred to allow influx of soil water carrying externally derived, dissolved U. Due to this influx, U precipitates along with newly formed clay minerals and oxyhydroxides in the rind. The conservative behavior of Th and the continuous addition of U into the rind adequately explain the observed systematic trends of ($^{238}\text{U}/^{232}\text{Th}$) and ($^{230}\text{Th}/^{232}\text{Th}$) activity ratios in the rind. Rind formation rates, determined from the measured U-series activity ratios with an open system U addition model, increase by a factor of ~ 1.3 (0.18–0.24 mm/kyr) from a low curvature to a high curvature section (0.018–0.12 mm⁻¹) of the core–rind boundary, revealing that curvature affects rates of rind formation as expected for diffusion-limited rind formation. U-series geochronometry thus provides the first direct evidence that the curvature of the interface controls the rate of regolith formation at the clast scale. The weathering rates determined at the clast scale can be reconciled with the weathering rates determined at the watershed or soil profile scale if surface roughness equals values of approximately 1300–2200.

© 2011 Elsevier Ltd. All rights reserved.

* Corresponding author at: Department of Geological Sciences, University of Texas at El Paso, El Paso, TX 79968-0555, USA. Tel.: +1 915 747 5218; fax: +1 915 747 5073.

E-mail address: lma@utep.edu (L. Ma).

1. INTRODUCTION

Weathering of silicate rocks plays many important roles in Earth surface processes, e.g., regulating atmospheric CO₂, providing nutrients to terrestrial ecosystem, and sculpting landscapes (e.g., Gilbert, 1877; Walker et al., 1981; Berner et al., 1983; Gaillardet et al., 1999; Kump et al., 2000; Anderson et al., 2002; Chadwick et al., 2003; Drever, 2004; Das et al., 2005; Hilley et al., 2010; Pogge von Strandmann et al., 2011). Despite covering only a small portion of the sub-aerially exposed area, small basaltic islands (e.g., Iceland, Azores, Reunion, Hawaii, Guadeloupe and volcanic arc islands) weather at rapid rates and could account for up to ~25% of CO₂ consumed by global silicate weathering (Louvat and Allegre, 1997; Gaillardet et al., 1999; Dessert et al., 2003). It is thus of great importance to quantify weathering rates of basaltic rocks and determine factors that control weathering reactions, especially for small basaltic islands in tropical climates where high temperature and precipitation accelerate soil formation processes (e.g., Chadwick et al., 2003, 2009). In such environments, rock fragments in the regolith zone commonly form alteration rinds. Such fragments or clasts consist of an unweathered core surrounded by a weathering rind: compared to the parent core, the rind is enriched in less mobile elements such as Ti, Fe, Th, and Al, and depleted in more mobile elements such as Mg, Ca, Na, and K (Cernohouz and Solc, 1966; Colman, 1982a,b; Sak et al., 2004, 2010; Navarre-Sitchler et al., 2011). Given that clasts within soils experience minimal physical erosion during weathering, these basaltic clasts in surficial weathering profiles provide simple and well-constrained systems to study chemical weathering processes for comparison to soil profile-scale or landscape-scale weathering. The comparison of weathering rates across different spatial scales has provided insights on understanding the factors that control chemical weathering (Navarre-Sitchler and Brantley, 2007).

The Uranium decay-series (U-series) includes radioactive isotopes of U, Th, and Ra that are characterized by various radioactive half-lives and geochemical properties. The fractionation of such isotopes occurs on various time scales in many geological environments (e.g., Ivanovich and Harmon, 1992; Bourdon et al., 2003). U-series isotopes have thus long been used as geochronologic tools for processes such as magmatic differentiation or deposition of carbonate rocks (Condomines et al., 2003; Edwards et al., 2003). Because of recent improved understanding of their behaviors during low temperature water–rock interaction, U-series isotopes (e.g., ²³⁸U, ²³⁴U, ²³⁰Th, and ²³²Th) in soils and riverine sediments have been shown to have great potential as a novel chronometer to constrain the rates and duration of chemical weathering at Earth's surface (Sarin et al., 1990; Chabaux et al., 2003a, 2008, 2011; Dosseto et al., 2008a,b; Granet et al., 2007, 2010; Ma et al., 2010). Recently, Pelt et al. (2008) determined formation rates of weathering rinds developed on basaltic composition clasts from Costa Rica using U-series isotopes. Such efforts show that U-series isotopes can quantify regolith formation as it relates to the creation and development of porosity in a low porosity rock (e.g., Fletcher et al., 2006; Navarre-Sitchler

et al., 2011). Furthermore, the application of U-series chronometry at the clast scale can be scaled to soil profiles and watersheds (Navarre-Sitchler and Brantley, 2007).

Often, thickness of rinds varies with the curvature of the rind–core boundary: in other words, rinds surround cores of unaltered protoliths that are more spherical than the original clasts (e. g., Cernohouz and Solc, 1966; Colman and Pierce, 1981; Oguchi, 2004; Sak et al., 2004, 2010; Kirkbride, 2005; Kirkbride and Bell, 2010). Sak et al. (2010) hypothesized that the curvature of the rind–core boundary controls the rates of chemical weathering reactions by governing the diffusive transport of reactants into the clast or products out of the clast: a higher curvature interface favors faster rind formation. In that effort, Sak et al. (2010) studied a single basaltic andesite clast from Basse-Terre Island in Guadeloupe. By using petrographic, bulk chemical, and electron microprobe analyses, Sak et al. (2010) documented the extent of weathering advance as a function of curvature. In that study, relative weathering rates increased with curvature but no independent age controls were available to quantify rates.

In this study, we analyze U-series isotopes and trace element concentrations to quantify rind formation rates on the same basaltic andesite weathering rind as previously studied in Guadeloupe (Sak et al., 2010). We present a quantitative model for weathering advance as a function of curvature for this clast and we compare it to weathering rates at the watershed scale.

2. GEOLOGICAL SETTING

The clast investigated here and in Sak et al. (2010) was collected from a thick (>8 m) regolith pile within the Bras David watershed on the French island of Basse-Terre, Guadeloupe in the Lesser Antilles (Fig. 1a). The rugged watershed is in a humid, tropical environment with a mean annual temperature of 25 °C and an annual precipitation up to 4500 mm (Lloret et al., 2011). The parent rock underlying the regolith is a late Quaternary volcanoclastic debris flow deposit of dominantly andesitic to basaltic composition (Samper et al., 2007). In this watershed, thick regolith profiles (>12 m) develop on the parent rock, which in this case is a volcanic debris flow deposit. The regolith is partially to completely depleted with respect to most primary minerals including pyroxene and feldspar as well as the glass matrix, and is enriched in Fe oxyhydroxides, gibbsite and kaolinite precipitates (Buss et al., 2010). The top of the regolith is a thin layer of soil. In the regolith that is exposed at roadcuts and excavations, rocky clasts at various stages of weathering are commonly observed.

One representative clast collected by Sak et al. (2010) in the B horizon of a soil profile at 0.8 m depth in the Bras David watershed was analyzed in this study (Fig. 1b). The clast sample is from a west-facing slope which is vegetated by grasses and widely dispersed trees. Volcanic flows in the immediate vicinity were emplaced 900 ka before present, based on Ar/Ar dating (Samper et al., 2007). The exposed debris flow deposits have experienced pedogenesis and become progressively more weathered toward the surface (Sak et al., 2010).

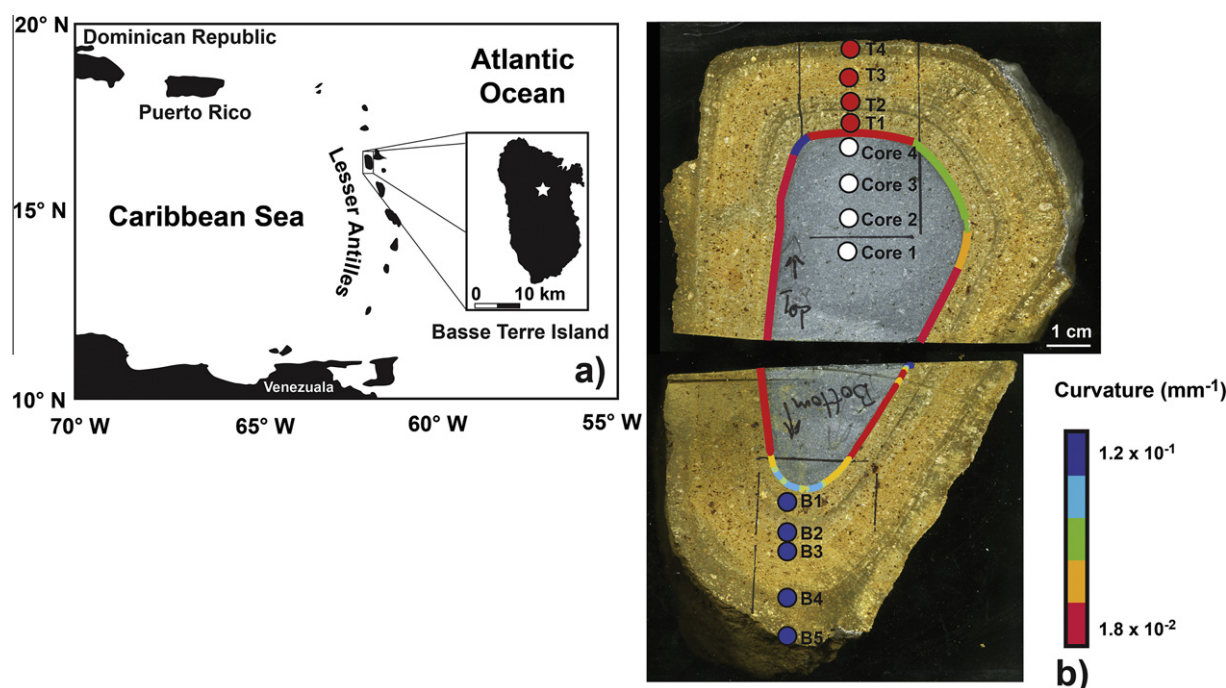


Fig. 1. (a) Location map of the Basse Terre Island in Guadeloupe. White star indicates the sample location in the Bras David watershed (after Sak et al., 2010); (b) Photographs of cut sections of the top and bottom segments, respectively. The visually defined core–rind boundary is color-coded for curvature (mm^{-1}) (after Sak et al., 2010). Drilled sample locations for the core (Core 1–Core 4), the top transect (T1–T4) and the bottom transect (B1–B5) are indicated. (For interpretation of the references to colour in this figure legend, the reader is referred to the web version of this article.)

3. METHODS

3.1. Field sampling and clast preparation

The clast was oriented and measured in the field prior to its removal from the outcrop. The weathering rind was distinguished from the surrounding soil by a difference in color: the rind is brownish yellow in contrast to the yellowish red matrix of the debris flow deposits. The original clast was about 15 cm long and 10 cm wide with an oblate shape. In the field, the major axis of this clast was oriented vertically, and the minor axis oriented horizontally (Fig. 1b). After extraction, the clast and attached rind were wrapped in plastic and masking tape and then were immersed in molten wax to preserve rind structure before returning to the laboratory. The wax-impregnated clast was separated into four sections by cutting a vertical section along the major axis and a perpendicular section through the minor axis (Fig. 1b).

The curvature of the core–rind boundary was determined and described in Sak et al. (2010). Briefly, the core–rind boundary was expressed as a series of (x, y) points on a scanned image of the cut section, where the color-change gradient was highest. The curvature (κ) of this boundary $y(x)$ was calculated using the following definition: $\kappa = y'' / (1 + (y')^2)^{3/2}$, where primes denote derivatives with respect to x . With this standard definition of curvature in two dimensions, only straight lines and circles have constant curvature. Note that we have defined the curvature as the curvature of the interface imaged in the plane of the clast slice (e.g., in two dimensions), and not the Laplacian

of the core–rind interface in three-dimensions. The measured curvature of the core–rind boundary is highest along the lower side of the clast (Fig. 1b).

The wax was subsequently removed prior to chemical analysis by heating to 55 °C for 8 h in an oven. Samples for chemical and isotopic analyses were obtained by drilling with a 3.175 mm diameter carbide-tipped bit to depth of 5–16 mm along linear profiles across the sliced clast (Fig. 1b). Four samples were collected from the core, four across the rind along a low curvature segment (the top transect) and five across the rind along a high curvature segment (the bottom transect) of the core–rind boundary (Fig. 1b). Additional core samples were prepared by grinding separate samples of core material.

3.2. Analytical methods for U–Th isotopes

About 20–100 mg powdered samples were weighed and spiked with a mixed artificial ^{233}U – ^{229}Th tracer for measurements of both U–Th isotopic compositions and concentrations. The samples were completely dissolved using a two-step procedure with HNO_3 – HF and HCl – H_3BO_3 acids. U and Th separation and purification were performed by conventional ion exchange chromatography. The whole procedure was developed at the Laboratoire d'Hydrologie et de Géochimie de Strasbourg (LHyGeS) in the University of Strasbourg, France (e.g., Granet et al., 2007; Pelt et al., 2008).

Briefly, U concentrations and ($^{234}\text{U}/^{238}\text{U}$) activity ratios (parenthesis means activity ratios hereafter) were analyzed using ~ 10 – 30 ng U. The measurements were performed on

a Thermal Ionization Mass Spectrometer (TIMS) Thermo-Scientific Triton. U concentrations were calculated using the measured $^{235}\text{U}/^{233}\text{U}$ isotopic ratios. ($^{234}\text{U}/^{238}\text{U}$) activity ratios were calculated using the analyzed $^{234}\text{U}/^{235}\text{U}$ ratios and assuming a constant $^{238}\text{U}/^{235}\text{U}$ ratio of 137.88, with the following decay constants: $\lambda_{238} = 1.551 \times 10^{-10} \text{ yr}^{-1}$ and $\lambda_{234} = 2.826 \times 10^{-6} \text{ yr}^{-1}$ (Akovali, 1994; Cheng et al., 2000). The precision and accuracy of the U activity ratios were determined from analyses of the HU1 standard solution (Cheng et al., 2000) and the basalt BEN rock standards (Govindaraju, 1994). During the measurement sessions, the mean of the HU1-standard analyses of ($^{234}\text{U}/^{238}\text{U}$) was 1.001 ± 0.004 ($n = 3$), in good agreement with the laboratory mean for 2009–2010 (0.999 ± 0.005 ; $n = 43$; 2σ) and consistent with secular equilibrium. In addition, two duplicates of the calcinated BEN rock standard, spiked with the ^{233}U – ^{229}Th tracer, were analyzed to yield a mean ($^{234}\text{U}/^{238}\text{U}$) of 1.001 ± 0.003 and a mean U concentration of 2.465 ± 0.008 ppm. Both values are consistent with previously published values from the same laboratory (in Ma et al., 2010) and with Govindaraju (1994). Several U measurements yielded low ^{234}U signal and high background noise due to low amounts of U available for analyses and hydrocarbon interferences from the wax in the rind sub-samples. For those measurements, internal errors (2SE) are greater than external error of the HU1 standard ($\sim 0.5\%$ 2SD). For those, we estimated an error of $\sim 1\%$ (e.g., Table 1).

$^{230}\text{Th}/^{232}\text{Th}$ isotopic ratios and Th concentrations were analyzed with ~ 50 ng Th (in ~ 50 ppb Th solutions), on a multiple collector inductively-coupled plasma mass spectrometer (MC-ICP-MS) Thermo-Finnigan Neptune. ^{230}Th and ^{229}Th were measured on the central SEM detector and ^{232}Th on a Faraday cup using the static collection mode. Concentrations of Th were determined using the measured $^{232}\text{Th}/^{229}\text{Th}$ isotopic ratios. The internal errors (2SE) of samples measurements are around 0.4% and 0.1% for $^{232}\text{Th}/^{230}\text{Th}$ and $^{232}\text{Th}/^{229}\text{Th}$ isotopic ratios, respectively. The standard-sample bracketing method was used to correct for a global measurement bias factor encompassing mass fractionation and the yield of the ion counter with an in-house ^{229}Th – ^{230}Th – ^{232}Th standard. The in-house Th standard was made from a mixture of the IRMM-035 Th standard with a certified value of $^{232}\text{Th}/^{230}\text{Th} = 87,100 \pm 592$, and a ^{229}Th spike solution. The $^{229}\text{Th}/^{230}\text{Th}$ ratio of the in-house standard was calibrated on the TIMS Triton using the peak jumping mode on the SEM. During the course of this study, the reproducibility and accuracy of Th isotopic ratio measurements was checked by regular analyses of the certified IRMM036 solution. The mean of 16 measurements gives $^{232}\text{Th}/^{230}\text{Th} = 323,283 \pm 2190$ (0.7%, 2σ) consistent with the IRMM certified value of $321,200 \pm 8000$ and with other laboratories (Sims et al., 2008). In addition, the two duplicates of the BEN rock standard were analyzed to yield a mean ($^{230}\text{Th}/^{238}\text{U}$) activity ratio of 1.01 ± 0.01 and a mean Th concentration of 10.5 ± 0.1 ppm. Both are consistent with secular equilibrium and previously published TIMS values from the same laboratory (in Ma et al., 2010).

The total procedure blanks for U–Th isotopic and elemental analysis are about ~ 10 pg for U and ~ 25 pg for Th. They were negligible ($< 0.7\%$) compared to the amount of U and Th analyzed in the samples. The ^{233}U – ^{229}Th tracer was regularly calibrated using TIMS with the ATTh rock standard. The wax used to encase the clast in the field was the same wax used in Pelt et al. (2008). According to Pelt et al. (2008), major and trace element contents (including U and Th) of the wax are insignificant and did not contaminate the subsamples.

3.3. Analytical methods for trace elements

About 30–80 mg powdered samples were used for measurements of trace element composition. The samples were completely dissolved using a two-step procedure with HNO_3 –HF and HCl – H_3BO_3 acids. Rare earth elements (REE), Y, Rb, Sr, and Ba concentrations were measured with ICP-MS (Thermo Fisher Scientific XS 2) at Pennsylvania State University. The sample trace element concentrations were calibrated using a series of element standards of known concentrations, prepared from NIST traceable High Purity Standards. Concentrations of rare earth element oxides relative to rare earth elements ($\text{REE}^+/\text{REE}^+$) as measured by the ICP-MS were optimized to be less than 1%, to minimize isobaric interferences. Detection limits were in the 0.1–1 ppt level for all trace elements reported here. To assess the analytical precision and accuracy, trace element concentrations were regularly measured for a basalt rock standard (USGS BHVO) and were generally within 3–7% of the reference values for REE, within 3% for Ba and Sr, and within 15% for Rb and Y.

4. RESULTS

Measured U and Th concentrations and activity ratios of the core and rind samples are listed in Table 1. Trace element concentrations for Ba, Rb, Sr, Y and REE of the core and the rind samples across the top (low curvature) transect are presented in Table 2. Major element chemistry of these clast samples has been previously measured and discussed by Sak et al. (2010) and is listed in Table 2 for reference.

4.1. Major and trace element profiles

To evaluate the loss or gain of elements in a weathering rind (especially to correct for relative concentration changes due to changes of other elements in the rind), concentration (C) of an immobile (i.e., conservative) element i is commonly used to compare with the relative loss or gain of a more mobile element (j) by calculating the open system mass transfer coefficient, $\tau_{i,j}$ (e.g., Brimhall and Dietrich, 1987; Anderson et al., 2002).

$$\tau_{i,j} = \frac{C_{j,w}}{C_{j,p}} \cdot \frac{C_{i,p}}{C_{i,w}} - 1 \quad (1)$$

Positive $\tau_{i,j}$ values indicate the extent of enrichment of element j and negative values define the fractional depletion with respect to the immobile element in the protolith. A value of zero means that element j is measured to be as immobile in

Table 1
U and Th concentrations and activity ratios in samples from the core, the top transect and the bottom transect.

Sample	Description	Distance* (mm)	U (ppm)	$\pm 2\sigma$	Th (ppm)	$\pm 2\sigma$	($^{234}\text{U}/^{238}\text{U}$)	$\pm 2\sigma$	($^{230}\text{Th}/^{232}\text{Th}$)	$\pm 2\sigma$	($^{238}\text{U}/^{232}\text{Th}$)	$\pm 2\sigma$	($^{230}\text{Th}/^{238}\text{U}$)	$\pm 2\sigma$
<i>Core samples</i>														
Core1	Drilled core	−23.0	0.332	0.002	1.041	0.011	0.999	0.005	0.969	0.004	0.967	0.010	1.002	0.012
Core3	Drilled core	−9.0	0.330	0.002	1.032	0.011	1.009	0.010	0.968	0.004	0.970	0.011	0.999	0.012
Core4	Drilled core	−2.0	0.338	0.002	1.045	0.011	1.003	0.005	0.973	0.003	0.980	0.011	0.993	0.012
CP1	Core powders	–	0.336	0.002	1.030	0.010	0.997	0.005	0.970	0.003	0.989	0.011	0.981	0.011
CP2	Core powders	–	0.326	0.002	1.026	0.011	1.003	0.005	0.977	0.003	0.964	0.011	1.013	0.012
CP3	Core powders	–	0.327	0.002	1.025	0.011	1.002	0.005	0.979	0.003	0.968	0.010	1.011	0.012
Average core			0.332		1.036		1.003		0.971		0.973		0.999	
<i>Top transect (low curvature)</i>														
T1	Drilled rind	2.0	0.737	0.004	1.917	0.020	1.031	0.010	0.988	0.008	1.167	0.013	0.847	0.012
T2	Drilled rind	5.8	0.741	0.004	1.810	0.019	1.012	0.010	1.010	0.008	1.243	0.014	0.812	0.011
T3	Drilled rind	12.8	0.907	0.005	1.906	0.020	1.011	0.010	1.063	0.006	1.444	0.016	0.736	0.010
T4	Drilled rind	19.8	1.211	0.007	2.022	0.021	1.016	0.010	1.349	0.005	1.817	0.020	0.743	0.009
<i>Bottom transect (high curvature)</i>														
B1	Drilled rind	2.2	0.878	0.005	2.286	0.021	1.009	0.010	0.997	0.008	1.165	0.013	0.856	0.012
B2	Drilled rind	8.0	0.936	0.005	2.221	0.021	1.003	0.005	1.025	0.008	1.279	0.013	0.802	0.012
B3	Drilled rind	14.5	1.122	0.005	2.285	0.021	1.009	0.005	1.112	0.008	1.490	0.013	0.746	0.012
B4	Drilled rind	22.7	1.225	0.005	2.200	0.021	1.001	0.005	1.303	0.008	1.690	0.013	0.771	0.012
B5	Drilled rind	29.9	1.284	0.005	2.194	0.021	1.015	0.005	1.375	0.008	1.776	0.013	0.774	0.012

Analytical errors are based on external reproducibility of synthetic solutions, rock standards and rock samples and are estimated to be 0.7% for U content and ($^{230}\text{Th}/^{232}\text{Th}$) isotopic ratios, 1% for Th content and ($^{238}\text{U}/^{232}\text{Th}$) ratios, and 1.5% for ($^{230}\text{Th}/^{238}\text{U}$) disequilibria. Parenthesis means activity ratios hereafter.

* Distance from core–rind boundary, positive sign indicates sample location in rind, negative sign indicates sample location in core.

Table 2
Trace and major element concentrations^a in samples from the core and the top transect.

Sample	Distance ^b (mm)	Ba (ppm)	Rb (ppm)	Sr (ppm)	La (ppm)	Ce (ppm)	Pr (ppm)	Nd (ppm)	Sm (ppm)	Eu (ppm)	Gd (ppm)	Tb (ppm)	Dy (ppm)	Ho (ppm)	Er (ppm)	Tm (ppm)	Yb (ppm)	Lu (ppm)	Y (ppm)	Al ₂ O ₃ (%)	CaO (%)	Fe ₂ O ₃ (%)	K ₂ O (%)	MgO (%)	MnO (%)	Na ₂ O (%)	SiO ₂ (%)	TiO ₂ (%)			
<i>Core samples</i>																															
Core1	-23.0	115	10.4	250	7.2	18	2.6	13.3	3.8	1.2	4.7	0.77	5.1	1.1	3.3	0.47	3.2	0.50	31.0	17.7	7.72	8.27	0.54	3.36	0.20	2.98	55.5	0.88			
Core2	-16.0	115	10.6	230	7.0	17.6	2.5	13.2	3.8	1.3	4.7	0.76	5.0	1.1	3.3	0.46	3.1	0.49	30.4	18.0	7.85	7.90	0.55	3.09	0.19	3.06	56.0	0.87			
Core3	-9.0	115	10.5	270	7.3	18.9	2.7	13.8	3.9	1.3	4.7	0.77	5.1	1.1	3.3	0.47	3.1	0.49	29.8	18.0	7.75	7.84	0.53	3.16	0.19	3.01	55.6	0.85			
Core4	-2.0	115	10.8	255	7.4	18.7	2.7	13.7	3.9	1.3	4.7	0.78	5.0	1.1	3.2	0.45	3.0	0.47	29.4	17.7	7.51	8.40	0.56	3.41	0.20	2.96	56.2	0.90			
Average core		115	10.6	251	7.2	18.3	2.6	13.5	3.9	1.3	4.7	0.77	5.1	1.1	3.3	0.46	3.1	0.49	30.2	17.9	7.71	8.10	0.55	3.26	0.20	3.00	55.8	0.88			
<i>Top transect (low altitude)</i>																															
T1	2.0	77.7	3.40	13.9	1.5	4.7	0.59	3.2	1.1	0.16	1.2	0.22	1.6	0.33	1.0	0.14	1.0	0.13	8.0	27.6	0.51	15.4	0.15	1.19	0.08	0.24	28.5	1.65			
T2	5.8	54.4	0.14	0.38	0.43	1.4	0.18	1.0	0.37	0.02	0.41	0.07	0.62	0.13	0.45	0.05	0.45	0.05	3.0	25.2	-0.02	15.4	-0.01	0.09	0.03	0.04	21.0	1.68			
T3	12.8	39.0	0.04	0.64	0.86	2.9	0.36	2.0	0.73	0.05	0.80	0.16	1.1	0.21	0.68	0.09	0.63	0.08	5.1	31.8	-0.02	16.3	-0.01	0.07	0.03	0.03	20.1	1.64			
T4	19.8	35.6	0.04	0.53	0.82	2.8	0.36	2.0	0.75	0.05	0.83	0.15	1.2	0.23	0.76	0.10	0.75	0.09	5.4	23.3	-0.02	15.3	-0.01	0.06	0.03	0.02	17.5	1.57			

^a Major element concentrations are from Sak et al. (2010).

^b Distance from core-rind boundary, positive sign indicates sample location in rind, negative sign indicates sample location in core.

the weathered rind (w) as the immobile element i with respect to parent material (p). In tropical weathering environments such as Guadeloupe, Ti is often found to be relatively immobile as its carrier phase such as ilmenite is generally stable (e.g., White et al., 1998; Sak et al., 2004, 2010; Buss et al., 2008, 2010). Leaching experiments with organic ligands at pH 6 also are consistent with Ti as the most immobile element during basalt dissolution, while Zr has been observed to be more immobile during granite leaching as its host mineral in granite is zircon (Neaman et al., 2006). Following Sak et al. (2010), $\tau_{i,j}$ values for the weathered clast are calculated assuming the parent composition is the average core composition (Table 2) and Ti is immobile. The chemical compositions of the four analyzed core samples are almost identical (Table 2), indicating that the core of the clast is homogenous.

The calculated $\tau_{Ti,j}$ values of the top transect rind samples for both major and trace elements are shown in Fig. 2. In this plot, the zero position along the transect was the core-rind boundary defined previously by the maximum gradient of color change on a scanned image of the clast (Sak et al., 2010). The $\tau_{Ti,j}$ values for elements such as Ca, Na, and Sr decrease abruptly from 0.0 to -1.0 across the core-rind interface (Fig. 2a), indicating complete loss of these elements in the rind. Such profiles in regolith are called *completely developed depletion profiles* (Brantley and White, 2009). In contrast, the $\tau_{Ti,j}$ values for K, Mg, Rb, Mn, Si, Ba, Al all show depletion profiles, but the lowest value of $\tau_{Ti,j}$ is greater than -1, so the depletion profile is *incompletely developed*, with the Al profile showing the least total extent of depletion at the outer rind boundary (ranging from a loss of 27% at the boundary to a possible gain of 4%, Fig. 2a). $\tau_{Ti,Fe}$ values remain relatively close to 0 across the rind (ranging from -0.01 to 0.07), indicating that Fe, like Ti, demonstrates an *immobile profile* (Brantley and White, 2009) during chemical weathering and rind formation. However, the slightly positive $\tau_{Ti,Fe}$ values may indicate that (i) Ti is slightly mobile relative to Fe, (ii) Fe is added to the weathering rinds via exogenous inputs, or (iii) heterogeneity of the protolith has introduced error into the calculation of $\tau_{Ti,Fe}$.

Negative $\tau_{Ti,REE}$ values across the weathering rind samples are consistent with significant loss of REE (Fig. 2b). In addition, core-normalized REE patterns of the rind samples show much more loss of Eu compared to REE neighbors such as Sm and Gd. Such a phenomenon is known as a negative Eu anomaly (Fig. 3; e.g., McLennan, 1989).

The $\tau_{Ti,Th}$ values of the weathering rind samples are close to 0 (ranging from -0.03 to 0.08) throughout the core into the rind (Fig. 4), in agreement with conservative (i.e. immobile) behavior for Th, similar to Ti (Fig. 2a). By contrast, the $\tau_{Ti,U}$ values increase continuously from 0 in the core to about ~ 1.2 in the rind (Fig. 4). Such a profile is termed an *addition profile* (Brantley and White, 2009) and is consistent with external addition of U (relative to Ti) into the rind during rind formation.

4.2. U and Th activity ratios

Measured U-series activity ratios of drilled core samples and core powders show very limited variations (Table 1), as

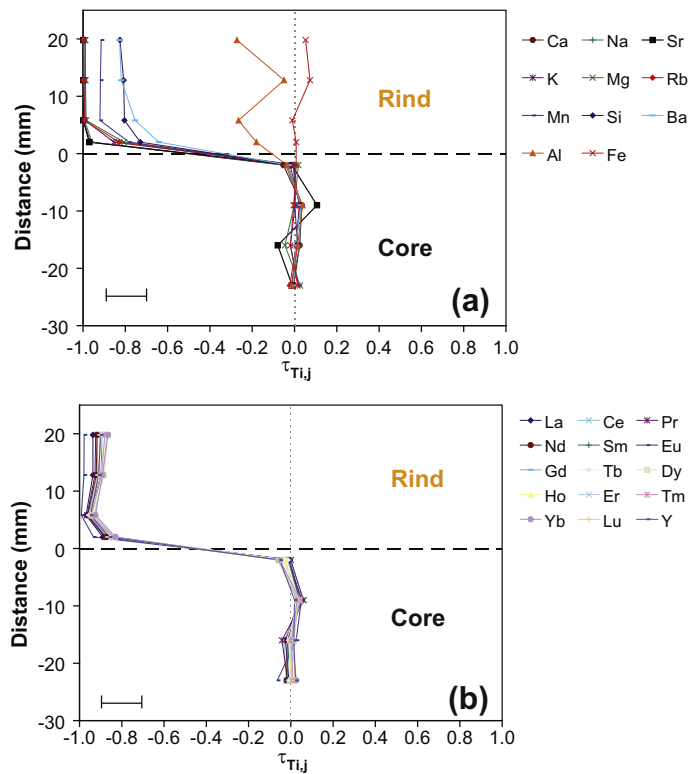


Fig. 2. Elemental mass transfer coefficients $\tau_{Ti,j}$ calculated using Eq. (1) plotted as a function of position relative to the core–rind boundary (indicated as position 0) for the top transect (low curvature site): (a) Major and trace elements; (b) Rare earth elements. The core–rind interface was defined following the same method in Sak et al. (2010). Values of $\tau_{Ti,j}$ are estimated to vary by $\sim 9\%$ as shown in the representative error bar due to variations in Ti and trace element measurements and parent heterogeneity.

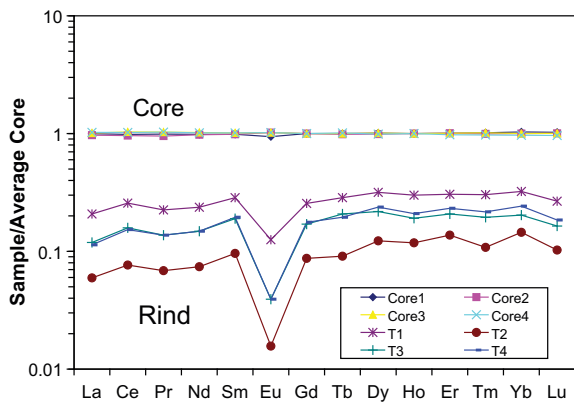


Fig. 3. Normalized rare earth element distribution patterns (normalized to average core composition; Table 2) of the core and rind samples from the top transect. Significant negative Eu anomalies, attributed to plagioclase dissolution, are observed in the rind samples. Relative errors are estimated to be $\sim 10\%$ from trace element measurements.

expected for a homogenous core. The average core activity ratios for ($^{234}\text{U}/^{238}\text{U}$), ($^{230}\text{Th}/^{232}\text{Th}$), ($^{238}\text{U}/^{232}\text{Th}$), and ($^{230}\text{Th}/^{238}\text{U}$) (parenthesis means activity ratios hereafter) are 1.003, 0.971, 0.973, and 0.999, respectively (Table 1). The activity ratios of ($^{234}\text{U}/^{238}\text{U}$) and ($^{230}\text{Th}/^{238}\text{U}$) are close

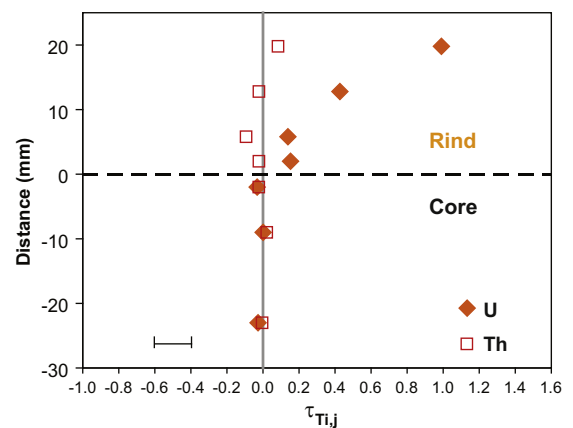


Fig. 4. Elemental mass transfer coefficients $\tau_{Ti,j}$ for U and Th plotted as a function of position relative to the core–rind boundary for the top transect (low curvature site). Values of $\tau_{Ti,j}$ are estimated to vary by $\sim 9\%$ as shown in the representative error bar due to variations in Ti and trace element measurements and parent heterogeneity.

to secular equilibrium within errors as expected from the 900 kyr old basaltic andesitic core.

In contrast, measured ($^{234}\text{U}/^{238}\text{U}$) activity ratios of the rind samples range from 1.011 to 1.031 for the top transect and from 1.001 to 1.015 for the bottom transect (Table 1;

Fig. 5a). Most of these values are higher than those of the core samples, showing excess ^{234}U relative to ^{238}U .

Measured ($^{238}\text{U}/^{232}\text{Th}$) activity ratios of these rind samples range from 1.167 to 1.817 for the top transect and from 1.165 to 1.776 for the bottom transect, all values significantly higher than the core samples (Table 1; Fig. 5b). Similarly, measured ($^{230}\text{Th}/^{232}\text{Th}$) activity ratios of these rind samples range from 0.988 to 1.349 for the top transect and from 0.997 to 1.375 for the bottom transect, also higher than the core samples (Table 1; Fig. 5c). More importantly, ($^{238}\text{U}/^{232}\text{Th}$) and ($^{230}\text{Th}/^{232}\text{Th}$) activity ratios increase continuously and systematically along both transect profiles, with distance increasing from the core into the rind (Fig. 5b and c).

5. DISCUSSION

5.1. Mobility of elements during rind formation

Elemental profiles measured on the top transect reveal that the extent of elemental loss across the core–rind interface (as measured in wt.%) decreases in the order $\text{Ca}, \text{Na}, \text{Sr} > \text{K}, \text{Mg}, \text{Rb} > \text{Mn} > \text{Si} > \text{Ba} > \text{Al} > \text{Fe}, \text{Ti}, \text{Th}$ (Fig. 2a; and Sak et al., 2010). Sak et al. (2010) discussed the major element depletion profiles for this transect and concluded that across the rind, primary minerals (plagioclase, pyroxene) and glass weather to Fe oxyhydroxides, gibbsite and minor kaolinite. They also concluded that the reactivity of phases in the clast decreases in the order $\text{plagioclase} \approx \text{pyroxene} \approx \text{glass matrix} > \text{apatite} \gg \text{ilmenite}$. The profiles measured here for Sr, Rb, Ba are consistent with that interpretation, where Sr is released from plagioclase and Rb and Ba are most likely released from pyroxene and glass (Fig. 2a). Petrologic studies have shown that Sr is particularly enriched in plagioclase (e.g., Berlin and Henderson, 1968) and Rb and Ba concentrations are high in volcanic glass matrix (e.g., Ewart et al., 1968). Furthermore, REE profiles show a significant negative Eu anomaly in the rind (Fig. 3), which documents loss of Eu as plagioclase dissolves early and completely during weathering. Plagioclase is known to be enriched in Eu compared to other REEs (e.g., McLennan, 1989).

The immobile profile documented by $\tau_{\text{Ti,Th}}$ across the top (low curvature) transect reveals the conservative behavior of Th (relative to Ti) during rind formation (Fig. 4), similar to that of Fe. Such an observation is consistent with the geochemical properties of Th: this element is generally immobile and particle-reactive during water–rock interaction due to the extremely low solubility of Th-containing phases (e.g., Rosholt et al., 1966; Latham and Schwarcz, 1987a,b; Gascoyne, 1992; Chabaux et al., 2003a). Similar conservative behavior of Th has been commonly observed for other cases of weathering in tropical climates such as Cameroon, China, and Costa Rica (Braun et al., 1993; Ma et al., 2007; Pelt et al., 2008).

Unlike Th and many other elements in this top transect, the U profile is consistent with the addition of U into the rind during clast weathering (Fig. 4). The almost linear increase of $\tau_{\text{Ti,U}}$ values and ($^{238}\text{U}/^{232}\text{Th}$) ratios with distance across the core–rind boundary into rind is consistent with continuous addition of U (Figs. 4 and 5b). Such continuous gains in U have been previously documented in soil profiles (Dequincey

et al., 2002; Chabaux et al., 2003b; Dosseto et al., 2008b; Ma et al., 2010), in river sediments (Andersson et al., 1998; Dosseto et al., 2006; Granet et al., 2007, 2010), and in the weathering basaltic clast studied in Costa Rica (Pelt et al., 2008). For the sites described in those studies, the U addition was interpreted as U precipitated or adsorbed from soil pore waters or river waters that contain high concentrations of U. U is mobilized in many soils during water–rock interactions under oxidizing conditions (e.g., Chabaux et al., 2003a). External addition of U is broadly consistent with the relatively soluble and mobile nature of U in the weathering environment (e.g., Chabaux et al., 2003a). U fixation is often attributed to co-precipitation or sorption of U onto secondary Fe-hydroxides or clay minerals when such minerals can provide a large surface area for sorption (Ames et al., 1983; Shirvington, 1983; Andersson et al., 1998; Duff et al., 2002; Chabaux et al., 2003a, 2008 and references therein). U immobilization is also likely when infiltrating porewaters become reducing because solubility of U-containing phases are lower under those conditions (Chabaux et al., 2003a, 2008 and references therein). Given that outer rind minerals are oxidized (e.g., Fe oxyhydroxides) and inner core minerals are reduced (pyroxene, ilmenite), it is likely that the activity of oxygen in fluids decreases with inward infiltration, lowering the solubility of U-containing phases and providing one reason why U precipitates near the core–rind interface. However, another mechanism may explain why U concentrations increase outward. Absorption or coprecipitation is likely as secondary Fe-hydroxides and clay minerals are observed to be abundant in the rind (Sak et al., 2010). The first reaction identified in the core of the Guadeloupe clast is oxidation of Fe in pyroxene; however significant porosity is generated only when plagioclase dissolution begins, slightly further out across the core–rind interface (Sak et al., 2010). The influx of soil water that carries dissolved U is readily explained by the increase in bulk porosity within the rind during chemical weathering of plagioclase; likewise, the increase in concentration of U outward is readily explained by the outward-increasing clay and Fe oxyhydroxide content.

5.2. ^{238}U – ^{234}U – ^{230}Th disequilibrium during rind formation

U-series activity ratios of the core samples display very little variation (Tables 1; Fig. 5) and are consistent with a homogenous core with respect to both elemental and isotopic composition (Table 2; Figs. 2–4). By contrast, U-series activity ratios of the rind samples are systematically different from those of core samples (e.g., $^{238}\text{U}/^{232}\text{Th}$ and $^{230}\text{Th}/^{232}\text{Th}$ activity ratios in Fig. 5). ($^{234}\text{U}/^{238}\text{U}$) activity ratios of the rind samples range from 1.001 and 1.031 and are generally >1 . U is soluble in water and importantly, compared to ^{238}U , ^{234}U is released to solution to greater extent. This preferential release occurs because ^{234}U is produced by alpha particle emission from ^{238}U decay and this alpha particle often damages the crystal lattice enabling preferential ^{234}U loss during water–rock interaction (Fleischer, 1980). For these reasons, fluid phases are generally characterized by ($^{234}\text{U}/^{238}\text{U}$) activity ratios >1 while residual solid materials that have recently been weathered are generally characterized by ($^{234}\text{U}/^{238}\text{U}$) activity ratios

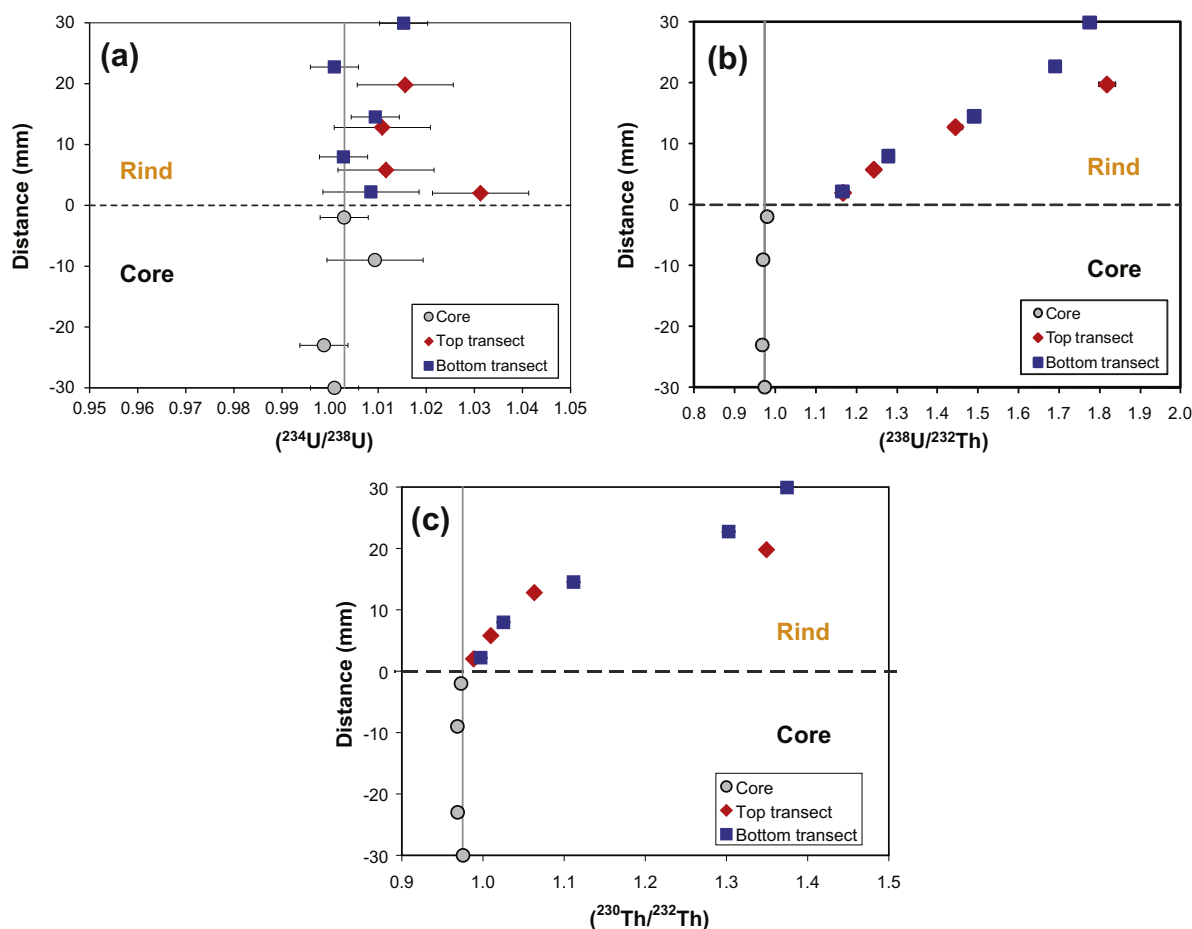


Fig. 5. Measured U–Th activity ratios, (a) $(^{234}\text{U}/^{238}\text{U})_a$; (b) $(^{238}\text{U}/^{232}\text{Th})_a$; (c) $(^{230}\text{Th}/^{232}\text{Th})_a$ plotted as a function of position relative to the core–rind boundary for the top transect (low curvature site) and the bottom transect (high curvature site). Grey lines indicate average core activity ratios (Table 1). Error bars in $(^{238}\text{U}/^{232}\text{Th})$ and $(^{230}\text{Th}/^{232}\text{Th})$ activity ratios are smaller than the size of symbols.

<1 (e.g., Rosholt et al., 1966; Vigier et al., 2001; Chabaux et al., 2003a, 2008; Dosseto et al., 2008a; Andersen et al., 2009). Lower ratios in solid materials can decay back to 1 only over timescales >1.25 Ma which is about 5 half-lives of the radioactive ^{234}U ($T_{1/2} = 244$ kyr). Although the observed $(^{234}\text{U}/^{238}\text{U})$ activity ratios in the weathering products (i.e., the rind) are only up to 3% away from secular equilibrium, the values are significantly greater than one (considering the errors of $^{234}\text{U}/^{238}\text{U}$ activity are generally ± 0.005 – 0.010). Values >1 differ from ratios expected for residual weathering products which would be <1 . This observation is consistent with addition of U as a precipitate or sorbate from soil pore waters during rind formation (Fig. 4). This addition of U into the rind is also supported by the positive $\tau_{\text{Th,U}}$ values.

Combined with the conservative behavior of Th, such a continuous addition of U (with excess ^{234}U over ^{238}U) is thus responsible for the observed gradual increase of $(^{238}\text{U}/^{232}\text{Th})$ activity ratios across the core–rind boundary for both the top and bottom rind transects (Fig. 5b). Over time, ^{238}U decays with a half-life ($T_{1/2}$) of ~ 4.5 Gyr to produce ^{234}U ($T_{1/2} = 244$ kyr), which in turn decays to ^{230}Th ($T_{1/2} = 75$ kyr). Hence, subsequent production of ^{230}Th from

excess ^{234}U in the rind accounts for the observed continuous increase of $(^{230}\text{Th}/^{232}\text{Th})$ activity ratios for both transects (Fig. 5c).

5.3. Rind formation rates calculated from ^{238}U – ^{234}U – ^{230}Th disequilibria

The use of U-series disequilibrium to constrain rind formation rates on a clast was first successfully applied to a clast from Costa Rica (Pelt et al., 2008). As in the clast studied here, Th showed conservative behavior and U was characterized by external addition. However, it was documented for the Costa Rica clast that U had been added to the rind mainly at the core–rind interface and that the rest of the rind did not show evidence for subsequent addition of U after the initial addition. In contrast, a continuous addition of U during rind formation is documented for the Guadeloupe clast (Figs. 4 and 5), and both $(^{238}\text{U}/^{232}\text{Th})$ and $(^{230}\text{Th}/^{232}\text{Th})$ activity ratios increase gradually across the core–rind boundary into the rind (Fig. 6). The explanation for the differences between these two U addition histories is probably related to different redox conditions or clay mineralogy. For example, perhaps U was added to the

Costa Rica clast only because of the redox change at the core–rind interface whereas U was added to the Guadeloupe clast mostly due to sorption onto secondary minerals. Under the open system conditions at Guadeloupe, the U-series isotopic variations in the rind over time can be modeled as continuous U addition and loss (Dequincey et al., 2002):

$$\frac{d^{238}\text{U}}{dt} = f_{238} - \lambda_{238}^{238}\text{U} - k_{238}^{238}\text{U} \quad (2)$$

$$\frac{d^{234}\text{U}}{dt} = f_{234} + \lambda_{238}^{238}\text{U} - \lambda_{234}^{234}\text{U} - k_{234}^{234}\text{U} \quad (3)$$

$$\frac{d^{230}\text{Th}}{dt} = \lambda_{234}^{234}\text{U} - \lambda_{230}^{230}\text{Th} \quad (4)$$

$$\frac{d^{232}\text{Th}}{dt} = -\lambda_{232}^{232}\text{Th} \quad (5)$$

Here, ^{238}U , ^{234}U , ^{230}Th , and ^{232}Th are the concentration terms (atoms g^{-1}); f_{238} and f_{234} are the input rates of ^{238}U and ^{234}U into the rind (atoms $\text{g}^{-1} \text{yr}^{-1}$). These terms lump together all the processes that add significant amounts of U-series isotopes into the rind material, except radioactive production and decay. The parameters k_{238} and k_{234} are first-order rate constants (yr^{-1}) for release of ^{238}U and ^{234}U from U-containing phases (Latham and Schwarcz, 1987a,b; Plater et al., 1992; Vigier et al., 2001), i.e. the rates that U-containing phases dissolve equal $k_{238}^{238}\text{U}$ or $k_{234}^{234}\text{U}$. In the model, these terms are considered to be constant with time for the purpose of simplicity and tractability (Ghaleb et al., 1990; Dequincey et al., 2002). The close-to-linear increase of $(^{238}\text{U}/^{232}\text{Th})_a$ ratios with distance from the core into the rind is consistent with a constant ^{238}U input rate in the model. Terms λ_{238} , λ_{234} , λ_{230} , and λ_{232} are the decay constants for ^{238}U , ^{234}U , ^{230}Th and ^{232}Th (yr^{-1}). For a given sample, the quantity t is the weathering exposure age (in years). Explicitly, “weathering exposure age” starts when the water–mineral interfacial area becomes large enough to mobilize measurable amounts of U-series isotopes. Calculated values of t increase with the position from the core–rind boundary into the rind. The point $t = 0$ is the point on the core–rind interface where no loss or gain of U-series isotopes is detected, identified here as the starting point of weathering. The term, $(\lambda_{234}/\lambda_{238})/(\lambda_{238}/\lambda_{238})$, represents the $(^{234}\text{U}/^{238}\text{U})$ activity ratio of the input source, e.g., the soil water, assuming that the deposition rates of ^{234}U and ^{238}U are identical. The term, k_{234}/k_{238} describes the relative rates of loss of ^{234}U to ^{238}U during leaching. Thus, the ratio k_{234}/k_{238} documents the ratio of the release rate of ^{234}U due to phenomena related to alpha particle damage to the crystal lattice (k_{234}) compared to the release rate due to congruent dissolution of the mineral (k_{238}).

With the measured $(^{238}\text{U}/^{232}\text{Th})_a$ and $(^{230}\text{Th}/^{232}\text{Th})_a$ activity ratios as input values and the average core U-series activity ratios as initial conditions (Table 1), the unknown parameters (f_{238} , f_{234} , and t) can be fully solved by using the Matlab™ *lsqnonlin* function (Appendix A).

In Fig. 6, the modeled data $(^{238}\text{U}/^{232}\text{Th})_a$, $(^{230}\text{Th}/^{232}\text{Th})_a$, $(^{234}\text{U}/^{238}\text{U})_a$, and $(^{230}\text{Th}/^{238}\text{U})_a$ plotted as curves) agree well with all the measured ratios except for one sample (sym-

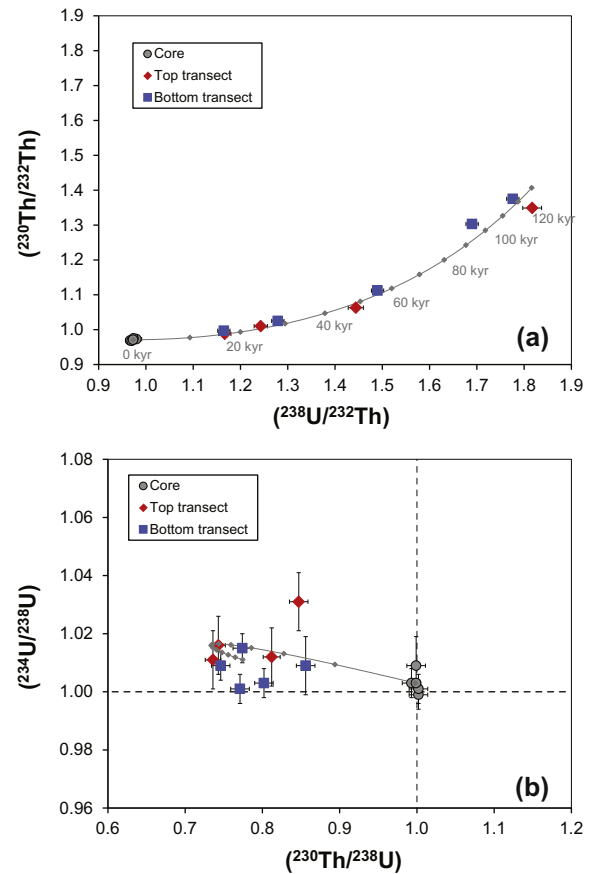


Fig. 6. **a)** $(^{230}\text{Th}/^{232}\text{Th})_a$ vs. $(^{238}\text{U}/^{232}\text{Th})_a$ isochron diagram; **(b)** $(^{230}\text{Th}/^{238}\text{U})_a$ vs. $(^{234}\text{U}/^{238}\text{U})_a$ ratios. Most of the analytical error bars are within the symbol size. Four out of five core samples are at secular equilibrium. The U–Th radioactive disequilibrium of the weathering rind samples from both transects is explained by (1) continuous input of U plus leaching of U starting at the core–rind boundary (without addition or loss of Th), and (2) subsequent production of ^{230}Th from U-series decay series in the rind. Rind formation ages were determined by an open-system U addition model (see text and appendix for details). When the model is solved, the activity ratios of $(^{238}\text{U}/^{232}\text{Th})_a$ and $(^{230}\text{Th}/^{232}\text{Th})_a$ as well as $(^{230}\text{Th}/^{238}\text{U})_a$ and $(^{234}\text{U}/^{238}\text{U})_a$ are calculated as a function of rind formation ages and are shown as the grey line.

bols). As expected, the weathering exposure ages for both transects increase with distance away from the core–rind boundary into the rind (Fig. 7). In addition the weathering exposure ages of the outermost samples from top and bottom are identical: e.g. ages of $\sim 121 \pm 8$ and $\sim 120 \pm 6$ kyr, respectively (Table 3). If we assume the rind grew at a rate that was constant in time, for example, to compare the average weathering advance rates for the two transects (e.g., Sak et al., 2004; Pelt et al., 2008), we use a linear regression to calculate the slope or rind formation rate, i.e., $\sim 0.18 \pm 0.07$ mm/kyr for the top profile and $\sim 0.24 \pm 0.02$ mm/kyr for the bottom profile (Fig. 7). It is worth noting here that the above rates represent weathering advance rates averaged over the entire ~ 120 ky weathering duration. However, the age–distance relationships show that the most recently weathered rind samples (e.g., samples

near core–rind boundary with ages $< \sim 60$ kyr) from both transects are consistent with similar rind formation rates (i.e., ~ 0.4 – 0.5 mm/kyr), while the samples in the outer rind – weathered in the more distant past – demonstrate different rates. Specifically, the rate is closer to ~ 0.10 mm/kyr (calculated from samples T3, T4) for the “instantaneous” rind formation over ~ 48 – 121 kyr for the top (low curvature) transect, and ~ 0.34 mm/kyr (calculated samples B4, B5) from 99 – 120 kyr for the bottom (high curvature) transect.

5.4. Control of curvature on rind formation rates

Previous studies have recognized that the thickness of rinds on weathered clasts vary with curvature of the weathering interface (e. g., Cernohouz and Solc, 1966; Colman and Pierce, 1981; Oguchi, 2004; Kirkbride, 2005; Kirkbride and Bell, 2010; Sak et al., 2010). However, some studies have shown that rind thickness does not vary as a function of clast size (Sak et al., 2004), depth within the weathering profile, or grain size of the core material (Navarre-Sitchler et al., 2011). On nonspherical clasts, rinds are often thicker near angular corners producing more rounded cores. In fact, the progressive rounding of corners has been used as an age indicator for weathering clasts (Cernohouz and Solc, 1966; Kirkbride and Bell, 2010).

The rind of the Guadeloupe clast similarly surrounds a core of unaltered material that is more spherical than the original clast (Fig. 1b), i.e., documenting that rind thickness increases with the curvature on the core–rind boundary. In fact, the average rind formation rate increases by a factor of about 1.3 (0.18 – 0.24 mm/kyr) from the low to high curvature transects where curvature changes by a factor of 6.7. In addition, the “instantaneous” rind formation rates for the outermost samples increases by a factor of about 3.6 (0.096 – 0.34 mm/kyr) from the low to high curvature sites while the more recent instantaneous rind formation rates are similar in the two regions. This latter observation is consistent with the fact that the core–rind boundary decreases in curvature over time as the core–rind interface becomes more spherical than the original clast.

The two outermost samples of the low and high curvature transects have U-series ages of 121 ± 8 and 120 ± 6 kyr, respectively, indicating that all the segments of the clast most likely experienced a similar weathering duration (age) (e.g., ~ 120 ka). The 120 kyr-long duration of chemical weathering inferred for the clast is consistent with the field observations that the regolith from Guadeloupe is depleted with respect to most primary minerals including pyroxene, feldspar and glass matrix, and is enriched in Fe oxyhydroxides, gibbsite and kaolinite precipitates (Buss et al., 2010). The emplacement age of the volcanic flows in the immediate vicinity of the study area is ~ 900 kyr (Samper et al., 2007). Apparently, although the lavas incorporated into the debris flow deposit were erupted ~ 900 kyr ago, the clast was exposed to weathering for a much shorter period of time.

Average rind formation rates can be calculated for any point on the clast by dividing rind thickness by the overall U-series determined weathering duration of the clast, 120 kyr. These calculated average rind formation rates (Fig. 8) show that weathering advance is not a function

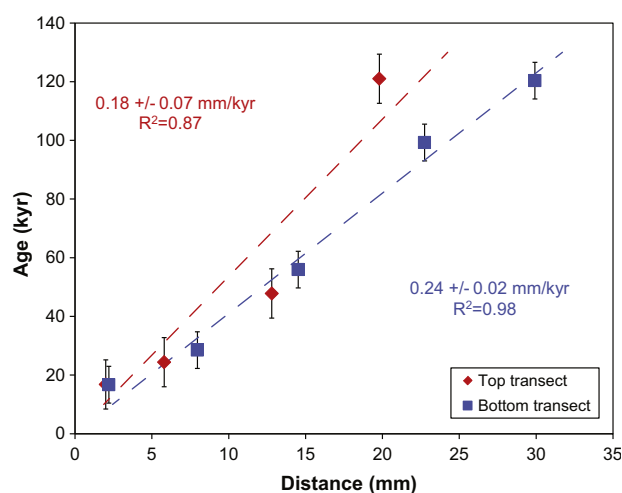


Fig. 7. Rind formation age (i.e., weathering exposure ages) plotted as a function of position relative to the core–rind boundary for the top transect (low curvature site) and the bottom transect (high curvature site). Dashed lines represent a linear regression to each transect. Regressions were forced through the origin as we define position 0 as the start point ($t = 0$) for chemical weathering. A rind formation rate of 0.18 ± 0.07 mm/kyr is inferred from the linear trend for the top transect and a rate of 0.24 ± 0.02 mm/kyr is inferred for the bottom transect. The oldest rind samples show rind formation rates, e.g., ~ 0.10 mm/kyr (calculated from samples T3, T4; corresponding to “in situ” rind formation from ~ 48 – 121 kyr), for the top transect and ~ 0.34 mm/kyr (calculated for samples B4, B5; corresponding to 99 – 120 kyr) for the bottom transect.

Table 3
Rind formation ages and model parameters determined from U-series disequilibrium.

Sample	Distance (mm)	Age (kyr)	\pm
<i>Top transect (low curvature)</i>			
T1	2.0	16.8	8.4
T2	5.8	24.3	8.4
T3	12.8	47.8	8.4
T4	19.8	121.0	8.4
<i>Bottom transect (high curvature)</i>			
B1	2.2	16.7	6.3
B2	8.0	28.5	6.3
B3	14.5	56.0	6.3
B4	22.7	99.3	6.3
B5	29.9	120.4	6.3
$f_{238}^{238}U_0$ (yr $^{-1}$)	$F^{234}U/F^{238}U$	$k^{238}U$	$k^{234}U/k^{238}U$
2.50×10^{-5}	1.07	1.19×10^{-5}	1.07

The model is solved as described in Appendix A. $^{238}U_0$ is initial number of ^{238}U atoms/g in the starting material of the system. All the other parameters are described as in the text.

of curvature below 0.1 mm^{-1} but increases with curvature at high curvature values (e.g., Sak et al., 2010), suggesting that the effects of curvature on weathering rates are most pronounced at high curvature sites.

Plagioclase dissolution is identified as the main process associated with significant pore formation in the rind material. A similar sequence of weathering reactions and

porosity development has also been observed in weathering basalt clasts from Costa Rica (Hausrath et al., 2008; Navarre-Sitchler et al., 2009). It was concluded in those earlier studies that while advective transport is likely to be important within the outermost sections of the rind where the porosity is high, the low porosity of the basaltic core and innermost rind materials precludes fast rates of advective transport. Therefore, the transport mechanism was inferred to be diffusion of reactants or products into or out of the core respectively. The observation of a higher rate of rind formation on a higher curvature interface is consistent with diffusion limiting weathering rind formation, as an increase in the fluxes of the components in the pore fluid at a higher curvature interface allows reactant to reach the weathering interface (or product to diffuse away) at higher rates than occurs at lower curvature, more planar sites. To explore this, Sak et al. (2010) developed a 2-D diffusion-limited model for a hypothetical angular clast in which a primary mineral phase reacts with a reactant aqueous species such as the proton to form a secondary mineral phase. In this model, the rind thickness increases as curvature increases (Sak et al., 2010). The rind formation rates determined here by U-series geochronometry provide the first direct evidence that the curvature of the interface controls the rate of the rind formation at the clast scale.

5.5. Comparison of chemical weathering rates to published estimates

The weathering advance rates of the Guadeloupe clast (0.18–0.24 mm/kyr) are within a factor of 3 of the rind formation rates (0.5 ± 0.2 mm/kyr) measured by using U-series isotopes on the basaltic clast from Costa Rica (Pelt et al., 2008). Such a consistency is most likely due to the similar tropical, wet climate and lithology. By contrast, basaltic rocks weathered more slowly under much colder and drier climate conditions, e.g., rind formation rates of ~ 0.01 – 0.02 mm/kyr were observed in Montana, Washington, and Idaho (Porter, 1975; Colman and Pierce, 1981). This comparison highlights the sensitivity of basaltic weathering rates under different climate regimes (e.g., temperature and precipitation, e.g., Das et al., 2005). An increase of weathering rates with temperature has also been observed in basalt dissolution experiments (e.g., Wolff-Boenisch et al., 2004; Hausrath and Brantley, 2010). The effect of climate on chemical weathering rates has long been demonstrated by examining dissolved loads from major rivers (Gaillardet et al., 1999), using cosmogenic nuclides and geochemical mass balance models for soil profiles (Riebe et al., 2004), compiling chemical and physical weathering rates from small catchments (West et al., 2005), and comparing plagioclase weathering rates across a climatic gradient in granitic terrain (Rasmussen et al., 2011).

The weathering rind formation rates determined by U-series isotopes in this study provide insights into basaltic weathering rates across different spatial scales. The unweathered core of the Guadeloupe clast has a bulk density of 2.7 g/cm³ and is composed of 9.6% K, Na, Ca, and Mg,

i.e., mobile elements that are readily lost to fluids during chemical weathering (Sak et al., 2010). Therefore, to compare this rind formation rate to weathering estimates at other scales of observation, we cast the average rind formation rates of ~ 0.18 – 0.24 mm/kyr as ~ 0.047 – 0.062 tons (Na + K + Mg + Ca)/km²_{clast area}/yr. This calculation entails the multiplication of the formation rate (in units of km/yr) by core density (in units of tons rock/km³). In turn, this rate in tons rock/km²/yr is then multiplied by the mass fraction of total cations (mass of Na + K + Mg + Ca lost from the rind/mass of rock). We implicitly assume that the weathering rates determined from this one clast are representative of the studied catchment.

No soil profile-scale observations of weathering advance rates are available in Guadeloupe. Nonetheless, catchment-wide chemical weathering rates have been calculated based on the chemistry of major elements in the Bras David streams at Guadeloupe (Rad et al., 2006; Gaillardet et al., accepted for publication). The soluble element load (Na + K + Ca + Mg) of the Bras David watershed after correction for atmospheric sea salt inputs ranges between 27 and 32 mg/l, which is equivalent to chemical weathering rates of 78–101 tons (Na + K + Ca + Mg)/km²_{catchment area}/yr, using mean runoff values of 2950–3750 mm/yr within the watershed (Gaillardet et al., accepted for publication).

These estimated weathering rates at the catchment scale are approximately 1300–2200 times faster than the weathering rates determined at the clast scale. The discrepancy in weathering rates may be contributed to the use of different “rulers” to normalize rates to unit area of the system (Navarre-Sitchler and Brantley, 2007). For example, the area of a watershed is measured at map scale and does not take into account all the roughness of the dissolving rock surface: this surface roughness includes roughness due to pyroclastic deposits containing volcanic material from ashes to blocks. Likewise, the map-scale roughness does not take into account the roughness at the scale of a clast or block. Navarre-Sitchler and Brantley (2007) showed that the rates of weathering for watersheds underlain by basalts are typically two orders of magnitude greater than weathering advance rates estimated for clasts (i.e., the relative roughness of the watershed weathering interface is 100× times that of the clast). As discussed by Sak et al. (2010), the weathering rates (tons/km²/yr) for the entire Bras David watershed can be reconciled with the clast weathering rate if roughness at the watershed scale equals values of approximately 1300–2200.

6. CONCLUSIONS

Weathering clasts are excellent “field sites” to study chemical weathering processes because the effects of physical erosion during their formation in the soil zone are minimized. For a basaltic andesite clast weathering in the Basse-Terre Island in Guadeloupe, elemental profiles reveal conservative behavior for Th but external addition of U to the rind relative to Ti during clast formation. In the rind, the sequence of weathering reactions includes

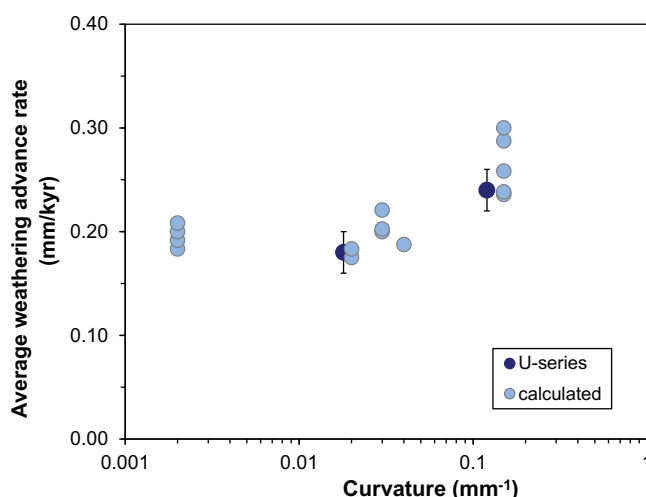


Fig. 8. Average weathering advance rate or rind formation rate plotted as a function of curvature of the visually defined core–rind boundary (curvature data from Sak et al., 2010). “U-series” indicate weathering rind formation rates that are determined by U-series disequilibrium in this study (Fig. 7). “Calculated” rates are inferred from the measured rind thickness at different segments of the clast (Sak et al., 2010) based on the assumption that the total weathering duration for the clast is 120 kyr (Table 3).

early pyroxene oxidation without observable pore formation followed by significant porosity formation due to plagioclase dissolution. The development of porosity is inferred to allow for influx of soil water which carries dissolved U. With this influx, U precipitates along with clay minerals and/or Fe oxyhydroxides in the rind. Combined with the conservative behavior of Th during clast weathering, the continuous addition of U into the rind is responsible for the observed systematic trends of U-series activity ratios such as ($^{238}\text{U}/^{232}\text{Th}$) and ($^{230}\text{Th}/^{232}\text{Th}$) across the core–rind boundary.

Based on the measured U-series activity ratios, rind formation rate can be determined. The rate increases by a factor of ~ 1.3 (0.18–0.24 mm/kyr) from a low curvature to a high curvature section (0.018–0.12 mm^{-1}) of the core–rind boundary, revealing that curvature affects rates of rind formation as expected for diffusion-limited rind formation. The weathering rates determined at the clast scale can be reconciled with the weathering rates at the watershed scale if surface roughness equals values of approximately 1300–2200. U-series geochronometry is thus proven to be an effective dating tool to study rind formation rates. This tool also quantifies how the curvature of the interface controls the rate of the regolith formation at the clast scale. Furthermore, this study highlights the potential for application of U-series dating technique in weathering clasts to examine the variations of chemical weathering rates along gradients of climate, topography and bedrock age and to compare rind formation rates with river-estimated rates of weathering to examine controls of hydrology, landscape, and scale on chemical weathering mechanisms. Further developments of this combined geochemical and isotopic approach will help to quantify rates of soil formation and landscape evolution across temporal and spatial scales, as well as project responses to future climate change and other anthropogenic impacts.

ACKNOWLEDGEMENTS

We would like to thank two anonymous reviewers for their constructive reviews, and Associate editor, Dr. E. Oelkers for his editorial handling and insightful review. This research was funded partially by the National Science Foundation Grant CHE-0431328 to S.L.B. for the Center for Environmental Kinetics Analysis at Pennsylvania State. In addition, S.L.B. acknowledges support for this weathering research from Department of Energy (DOE) Grant DE-FG02-05ER15675. Additional funding from the University of Strasbourg (France) and from Alsace Region (REALISE work) is graciously acknowledged. Waleska Castro (PSU) assisted in the laboratory, Celine Dessert (IPGP), and Emily Lloret (IPGP) assisted in the field, and L’Observatoire Volcanologique et Sismologique de Guadeloupe (IPGP) provided logistical support. L.M. also acknowledges support from Center of Earth and Environmental Isotope Research at UTEP.

APPENDIX A. SOLVING THE CONTINUOUS U ADDITION MODEL

We present here a solution to the continuous U addition and loss model. The model consists of the system of Eqs. (2)–(5) for weathering exposure ages (t), input rates of ^{238}U and ^{234}U (f_{238} and f_{234}) and leaching coefficients of ^{234}U and ^{238}U (k_{234} and k_{238}). These values were derived to best reproduce the measured ($^{238}\text{U}/^{232}\text{Th}$), ($^{230}\text{Th}/^{232}\text{Th}$), and ($^{234}\text{U}/^{238}\text{U}$) activity ratios as a function of time.

The ordinary differential Eqs. (2)–(5) were first solved analytically and rearranged to describe ($^{238}\text{U}/^{232}\text{Th}$), ($^{230}\text{Th}/^{232}\text{Th}$), and ($^{234}\text{U}/^{238}\text{U}$) activity ratios for a weathering rind sample as a function of f_{238} , f_{234} , k_{234} , k_{238} , and t (Eqs. (A1)–(A3)):

$$\left(\frac{^{238}\text{U}}{^{232}\text{Th}}\right)_a = \left(\frac{^{238}\text{U}}{^{232}\text{Th}}\right)_0 \left[\left(1 - \frac{f_{238}}{^{238}\text{U}_0 a_{238}}\right) e^{(\lambda_{232} - a_{238})t} + \frac{f_{238}}{^{238}\text{U}_0 a_{238}} e^{\lambda_{232}t} \right] \quad (\text{A1})$$

$$\begin{aligned} \left(\frac{^{230}\text{Th}}{^{232}\text{Th}}\right)_a &= \left(\frac{^{230}\text{Th}}{^{232}\text{Th}}\right)_0 e^{(\lambda_{232}-\lambda_{230})t} + \left(\frac{^{238}\text{U}}{^{232}\text{Th}}\right)_0 \\ &\times \frac{\lambda_{230}\lambda_{234}}{\lambda_{230}-a_{234}} (e^{-a_{234}t} - e^{-\lambda_{230}t}) e^{\lambda_{232}t} \\ &\times \left[\left(\frac{^{234}\text{U}}{^{238}\text{U}}\right)_0 \frac{1}{\lambda_{234}} - \frac{f_{234}}{\lambda_{238}\lambda_{234}a_{238}} + \frac{f_{238}}{\lambda_{238}\lambda_{234}a_{238}} - \frac{a_{238}}{a_{238}(a_{234}-a_{238})} \right] \\ &+ \left(\frac{^{238}\text{U}}{^{232}\text{Th}}\right)_0 \frac{\lambda_{230}\lambda_{234}}{\lambda_{230}-a_{238}} (e^{-a_{238}t} - e^{-\lambda_{230}t}) e^{\lambda_{232}t} \frac{a_{238}-f_{238}}{a_{238}(a_{234}-a_{238})} \\ &+ \left(\frac{^{238}\text{U}}{^{232}\text{Th}}\right)_0 \lambda_{234} \frac{f_{234}a_{238} + f_{238}\lambda_{238}}{a_{234}a_{238}\lambda_{238}} (1 - e^{-\lambda_{230}t}) e^{\lambda_{232}t} \quad (\text{A2}) \end{aligned}$$

$$\left(\frac{^{234}\text{U}}{^{238}\text{U}}\right)_a = \left\{ \left[\left(\frac{^{234}\text{U}}{^{238}\text{U}}\right)_0 - \frac{\lambda_{234} \left(\frac{f_{234}a_{238}}{\lambda_{238}\lambda_{234}a_{238}} + \frac{f_{238}a_{238}}{\lambda_{238}\lambda_{234}a_{238}} \right)}{a_{234}a_{238}\lambda_{238}} - \frac{\lambda_{234} \left(a_{238} - \frac{f_{238}}{\lambda_{238}\lambda_{234}a_{238}} \right)}{(a_{234}-a_{238})a_{238}} \right] e^{-a_{234}t} \right\} / \left\{ \left(1 - \frac{f_{238}}{\lambda_{238}\lambda_{234}a_{238}} \right) e^{-a_{238}t} + \frac{f_{238}}{\lambda_{238}\lambda_{234}a_{238}} \right\} \quad (\text{A3})$$

$$a_{238} = \lambda_{238} + k_{238}$$

$$a_{234} = \lambda_{234} + k_{234}$$

where $(^{238}\text{U}/^{232}\text{Th})_0$, $(^{234}\text{U}/^{238}\text{U})_0$ and $(^{230}\text{Th}/^{232}\text{Th})_0$ are initial activity ratios for the unweathered core; $^{238}\text{U}_0$ is the initial concentration of ^{238}U (atoms/g) in the starting material.

For both rind transects, measured $(^{238}\text{U}/^{232}\text{Th})$, $(^{230}\text{Th}/^{232}\text{Th})$, and $(^{234}\text{U}/^{238}\text{U})$ activity ratios in each rind sample are used to constrain the model. The average core composition (Table 1) was used to represent the starting material. To solve the model equations, we assume the input terms (f_{238} , f_{234} , k_{238} and k_{234}) are constant over the rind over time.

The model is constrained by 27 observations for the top and bottom transects ($^{238}\text{U}/^{232}\text{Th}$, $^{230}\text{Th}/^{232}\text{Th}$ and $^{234}\text{U}/^{238}\text{U}$ activity ratios from nine samples as data). The model fits 13 parameters (nine ages and f_{238} , f_{234} , k_{238} , k_{234}) to data describing the two profiles. The number of model equations is greater than the number of unknowns, and thus the model is over-determined. The unknown parameters were solved in a similar manner to that of Dosseto et al. (2008b) and Ma et al. (2010) as described below.

Best-fit parameters were calculated with the MatlabTM *lsqnonlin* function (version 7.1), which uses a large-scale algorithm to solve nonlinear least-squares problems. This function searches for the vector v that minimizes the sum of the square of the difference between observed and modeled values for U-series activity ratios. The solution yields a function $f(v)$ whose m components are the constraining equations of U-series activity ratios. The calculation is initiated with an initial value v_0 , provided randomly. Specifically, v is the vector of output parameters (nine ages and f_{238} , f_{234} , k_{238} , k_{234}) and the components of $f(v)$ are the measured $(^{238}\text{U}/^{232}\text{Th})$, $(^{230}\text{Th}/^{232}\text{Th})$, and $(^{234}\text{U}/^{238}\text{U})$ activity ratios. The algorithm calculates output parameters for any v values and seeks the value of v that best fits the observed activity ratios. For all the trials with random initial value v_0 , the function only returns one unique set of solutions. Thus no error estimates on the returned parameters are available. Instead, the error on the age was evaluated

by two methods. The first method involved error propagation using a Monte Carlo simulation (e.g., Pelt et al., 2008), that took into account the uncertainties in measured activity ratios. The uncertainty in age from this method is about ± 4 ka (2σ). The second method incorporated the observation that the drill core has an approximate radius of 1.5 mm. Given that the rind formation rates were 0.18–0.24 mm/kyr, the radius of the drill core corresponds to an error in the age measurement of ± 6.3 –8.4 ka. Hence the age precision is set as ± 6.3 –8.4 ka for all drilled samples (Table 3).

REFERENCES

- Akovali Y. A. (1994) Nuclear data sheets for A = 234. *Nucl. Data Sheets* **71**, 18.
- Ames L. L., McGarrath J. E. and Walker B. A. (1983) Sorption of trace constituents from aqueous solutions onto secondary minerals. I Uranium. *Clay Clay Mineral.* **31**, 321–334.
- Andersson P. S., Porcelli D., Wasserburg G. J. and Ingri J. (1998) Particle transport of ^{234}U – ^{238}U in the Kalix River and in the Baltic Sea. *Geochim. Cosmochim. Acta* **62**, 385–392.
- Anderson S. P., Dietrich W. E. and Brimhall G. H. (2002) Weathering profiles, mass-balance analysis, and rates of solute loss: linkage between weathering and erosion in a small, steep catchment. *Geol. Soc. Am. Bull.* **114**, 1143–1158.
- Andersen M. B., Erel Y. and Bourdon B. (2009) Experimental evidence for ^{234}U – ^{238}U fractionation during granite weathering with implications for $^{234}\text{U}/^{238}\text{U}$ in natural waters. *Geochim. Cosmochim. Acta* **73**, 4124–4141.
- Berlin R. and Henderson C. M. B. (1968) A reinterpretation of Sr and Ca fractionation trends in plagioclases from basic rocks. *Earth Planet. Sci. Lett.* **4**, 179–183.
- Berner R. A., Lasaga A. and Garrels R. M. (1983) The carbonate-silicate geochemical cycle and its effect on atmospheric carbon dioxide over the past 100 million years. *Am. J. Sci.* **283**, 641–683.
- Bourdon B., Henderson G. M., Lundstrom C. C. and Turner S.P. (2003) Uranium-series Geochemistry, *Rev. Mineral. Geochem.* **52**. Mineralogical Society of America, Washington, DC, 656 pp.
- Brantley S. L. and White A. F. (2009) Approaches to modeling weathered regolith. *Rev. Mineral. Geochem.* **70**, 435–484.
- Braun J.-J., Pagel M., Herbillion A. and Rosin C. (1993) Mobilization and redistribution of REEs and thorium in a syenitic lateritic profile: a mass balance study. *Geochim. Cosmochim. Acta* **57**, 4419–4434.
- Brimhall G. H. and Dietrich W. E. (1987) Constitutive mass balance relations between chemical composition, volume, density, porosity, and strain in metosomatic hydrochemical systems: results on weathering and pedogenesis. *Geochim. Cosmochim. Acta* **51**, 567–587.
- Buss H. L., Sak P. B., Webb S. M. and Brantley S. L. (2008) Weathering of the Rio Blanco quartz diorite, Luquillo Mountains, Puerto Rico: coupling oxidation, dissolution, and fracturing. *Geochim. Cosmochim. Acta* **72**, 4488–4507.

- Buss H. L., White A. F., Dessert C., Gaillardet, J., Blum A. E. and Sak P. B. (2010) Depth profiles in a tropical, volcanic critical zone observatory: Basse-Terre, Guadeloupe. In *Proceedings of the 13th International Symposium on Water–Rock Interaction* (eds. I. S. Torres-Alvarado, P. Birkkale).
- Cernohou J. and Solc I. (1966) Use of sandstone wanes and weathered basaltic crust in absolute chronology. *Nature* **212**, 806–807.
- Chabaux F., Riotte J. and Dequincey O. (2003a) U–Th–Ra fractionation during weathering and river transport. *Rev. Mineral. Geochem.* **52**, 533–576.
- Chabaux F., Dequincey O., Levesque J.-J., Leprun J.-C., Clauer N., Riotte J. and Paquet H. (2003b) Tracing and dating recent chemical transfers in weathering profiles by trace element geochemistry and ^{238}U – ^{234}U – ^{230}Th disequilibria: the example of the Kaya lateritic toposequence (Burkina-Faso). *C. R. Geosci.* **335**, 1219–1231.
- Chabaux F., Bourdon B. and Riotte J. (2008) U-series geochemistry in weathering profiles, river waters and lakes. *Radioactiv. Environ.* **13**, 49–104.
- Chabaux F., Ma L., Stille P., Pelt E., Granet M., Lemarchand D., Chiara Roupert R. and Brantley S. L. (2011) Determination of chemical weathering rates from U series nuclides in soils and weathering profiles: principles, applications and limitations. *Appl. Geochem.* **26**, S20–S23.
- Chadwick O. A., Gavenda R. T., Kelly E. F., Ziegler K., Olson C. G., Elliot W. C. and Hendricks D. M. (2003) The impact of climate on the biogeochemical functioning of volcanic soils. *Chem. Geol.* **202**, 195–223.
- Chadwick O. A., Derry L. A., Bern C. R. and Vitousek P. M. (2009) Changing sources of strontium to soils and ecosystems across the Hawaiian Islands. *Chem. Geol.* **267**, 64–76.
- Cheng H., Edwards R. L., Hoff J., Gallup C. D., Richards D. A. and Asmerom Y. (2000) The half-lives of uranium-234 and thorium-230. *Chem. Geol.* **169**, 17–33.
- Colman S. M., and Pierce K. L. (1981) Weathering rinds on andesitic and basaltic stones as a Quaternary age indicator. Western United States. *US Geological Survey Professional Paper*. 41p.
- Colman S. M. (1982a) Clay mineralogy of weathering rinds and possible implications concerning the sources of clay minerals in soil. *Geology* **10**, 370–375.
- Colman S. M. (1982b) Chemical weathering of basalts and basaltic andesites: evidence from weathering rinds. *USGS Professional Paper* 1210. 51p.
- Condomines M., Gauthier P.-J. and Sigmarsson O. (2003) Timescales of magma chamber processes and dating of young volcanic rocks. *Rev. Mineral. Geochem.* **52**, 125–174.
- Das A., Krishnaswami S., Sarin M. M. and Pande K. (2005) Chemical weathering in the Krishna Basin and Western Ghats of the Deccan Traps, India: rates of basalt weathering and their controls. *Geochim. Cosmochim. Acta* **69**, 2067–2084.
- Dequincey O., Chabaux F., Clauer N., Sigmarsson O., Liewig N. and Leprun J.-C. (2002) Chemical mobilizations in laterites: evidence from trace elements and ^{238}U – ^{234}U – ^{230}Th disequilibria. *Geochim. Cosmochim. Acta* **66**, 1197–1210.
- Dessert C., Dupre B., Gaillardet J., Francois L. M. and Allegre C. J. (2003) Basalt weathering laws and the impact of basalt weathering on the global carbon cycle. *Chem. Geol.* **202**, 257–273.
- Dosseto A., Bourdon B., Gaillardet J., Allegre C. J. and Filizola N. (2006) Timescale and conditions of chemical weathering under tropic climate: study of the Amazon basin with U-series. *Geochim. Cosmochim. Acta* **70**, 71–89.
- Dosseto A. D., Bourdon B. and Turner S. P. (2008a) Uranium-series isotopes in river materials: insights into the timescales of erosion and sediment transport. *Earth Planet. Sci. Lett.* **265**, 1–17.
- Dosseto A., Turner S. P. and Chappell J. (2008b) The evolution of weathering profiles through time: new insights from uranium-series isotopes. *Earth Planet. Sci. Lett.* **274**, 359–371.
- Drever J. I. (2004) Surface and ground water, weathering, and soils. In *Treatise on Geochemistry*, vol. 5 (eds. H. D. Holland and Turekian). Elsevier, San Diego, CA, 626 pp.
- Duff M. C., Coughlin J. U. and Hunter D. B. (2002) Uranium coprecipitation with iron oxide minerals. *Geochim. Cosmochim. Acta* **66**, 3533–3547.
- Edwards R. L., Gallup C. D. and Cheng H. (2003) Uranium-series dating of marine and lacustrine carbonates. *Rev. Mineral. Geochem.* **52**, 363–405.
- Ewart A., Taylor S. R. and Capp A. C. (1968) Trace and minor element geochemistry of the rhyolitic volcanic rocks, Central North Island, New Zealand. *Contrib. Mineral. Petrol.* **18**, 76–104.
- Fleischer R. L. (1980) Isotopic disequilibrium of uranium: alpha-recoil damage and preferential solution effects. *Science* **207**, 979–981.
- Fletcher R. C., Buss H. L. and Brantley S. L. (2006) A spheroidal weathering model coupling porewater chemistry to soil thickness during steady-state denudation. *Earth Planet. Sci. Lett.* **244**, 444–457.
- Gaillardet J., Dupre B., Louvat P. and Allegre C. J. (1999) Global silicate weathering and CO_2 consumption rates deduced from the chemistry of large rivers. *Chem. Geol.* **159**, 3–30.
- Gaillardet J., Rad S., Rivé K., Louvat P., Gorge C., Allègre C. and Lajeunesse E. (accepted for publication), Orography-driven chemical denudation in the Lesser Antilles: evidence for a new feedback mechanism stabilizing atmospheric CO_2 . *Am. J. Sci.*
- Gascoyne M. (1992) Geochemistry of the actinides and their daughters. In *Uranium-Series Disequilibrium: Application to Earth, Marine, and Environmental Sciences* (eds. M. Ivanovich and R. S. Harmon). Oxford Sciences Publications, Oxford, pp. 34–61.
- Ghaleb B., Hillaire-Marcel C., Causse C., Gariépy C. and Vallières S. (1990) Fractionation and recycling of U and Th isotopes in a semiarid endoreic depression of central Syria. *Geochim. Cosmochim. Acta* **54**, 1025–1035.
- Gilbert G. K. (1877), *Report on the Geology of the Henry Mountains*. US Geographical and Geological Survey, Rocky Mountains region. 170 p.
- Govindaraju K. (1994) Compilation of working values and sample description for 383 geostandards. *Geostand. Newlett.* **18**(S1), 1–158.
- Granet M., Chabaux F., Stille P., France-Lanord C. and Pelt E. (2007) Time-scales of sedimentary transfer and weathering processes from U-series nuclides: clues from the Himalayan rivers. *Earth Planet. Sci. Lett.* **261**, 389–406.
- Granet M., Chabaux F., Stille P., Dosseto A., France-Lanord C. and Blaes E. (2010) U-series disequilibria in suspended river sediments and implication for sediment transfer time in alluvial plains: the case of the Himalayan rivers. *Geochim. Cosmochim. Acta* **74**, 2851–2865.
- Hausrath E. M., Navarre-Sitchler A., Sak P. B., Steefel C. I. and Brantley S. L. (2008) Basalt weathering rates on Earth and the duration of liquid water on the plains of Gusev Crater. *Mars. Geol.* **36**, 67–70.
- Hausrath E. M. and Brantley S. L. (2010) Basalt and olivine dissolution under cold, salty, and acidic conditions: what can we learn about recent aqueous weathering on Mars? *J. Geophys. Res.* **115**, E12001. doi:10.1029/2010JE003610.
- Hilley G. E., Chamberlain C. P., Moon S. G., Porder S. and Willett S. (2010) Competition between erosion and reaction kinetics in controlling silicate weathering rates. *Earth Planet. Sci. Lett.* **293**, 191–199.

- Ivanovich M. and Harmon R. S. (1992) *Uranium-series Disequilibrium: Applications to Earth, Marine, and Environmental Sciences*. Clarendon Press, Oxford.
- Kirkbride M. P. (2005) Boulder edge-roundness as an indicator of relative age: a Lochnagar case study. *Scott. Geog. J.* **121**, 219–236.
- Kirkbride M. P. and Bell C. M. (2010) Edge-roundness of boulders of Torridonian Sandstone (northwest Scotland): applications for relative dating and implications for warm and cold climate weathering rates. *Boreas* **39**, 187–198.
- Kump L. R., Brantley S. B. and Arthur M. A. (2000) Chemical weathering, atmospheric CO₂, and climate. *Annu. Rev. Earth Planet. Sci.* **28**, 611–667.
- Latham A. G. and Schwarcz H. P. (1987a) On the possibility of determining rates of removal of uranium from crystalline igneous rocks using U-series disequilibria – 1: a U-leach model, and its applicability to whole-rock data. *Appl. Geochem.* **2**, 55–65.
- Latham A. G. and Schwarcz H. P. (1987b) On the possibility of determining rates of removal of uranium from crystalline igneous rocks using U-series disequilibria – 2: applicability of a U-leach model to mineral separates. *Appl. Geochem.* **2**, 67–71.
- Louvat P. and Allegre C. J. (1997) Present denudation rates on the island of Reunion determined by river geochemistry: basalt weathering and mass budget between chemical and mechanical erosions. *Geochim. Cosmochim. Acta* **61**, 3645–3669.
- Lloret E., Dessert C., Gaillardet J., Alberic P., Crispi O., Chaduteau C. and Benedetti M. F. (2011) Comparison of dissolved inorganic and organic carbon yields and fluxes in the watersheds of tropical volcanic islands, examples from Guadeloupe (French West Indies). *Chem. Geol.* **280**, 65–78.
- Ma J.-L., Wei G.-J., Xu Y.-G., Long W.-G. and Sun W.-D. (2007) Mobilization and re-distribution of major and trace elements during extreme weathering of basalt in Hainan Island, South China. *Geochim. Cosmochim. Acta* **71**, 3223–3237.
- Ma L., Chabaux F., Pelt E., Blaes E., Jin L. and Brantley S. L. (2010) Regolith production rates calculated with uranium-series isotopes at Susquehanna/Shale Hills Critical Zone Observatory. *Earth Planet. Sci. Lett.* **297**, 211–225.
- McLennan S. M. (1989) Rare earth elements in sedimentary rocks: influence of provenance and sedimentary processes. *Rev. Mineral.* **21**, 169–200.
- Navarre-Sitchler A. K. and Brantley S. L. (2007) Basalt weathering across scales. *Earth Planet. Sci. Lett.* **261**, 321–334.
- Navarre-Sitchler A., Steefel C., Tomutsa L., Yang L. and Brantley S. L. (2009) Evolution of porosity and diffusivity during chemical weathering of a basalt clast. *J. Geophys. Res. Earth Surf.* **114**, F02016. doi:10.1029/2008JF001060.
- Navarre-Sitchler A., Steefel C., Sak P. and Brantley S. L. (2011) A reactive-transport model for weathering rind formation on basalt. *Geochim. Cosmochim. Acta* **75**, 7644–7667.
- Neaman A., Chorover J. and Brantley S. L. (2006) Effects of organic ligands on granite dissolution in batch experiments at pH 6. *Am. J. Sci.* **306**, 451–473.
- Oguchi C. T. (2004) A porosity-related diffusion model of weathering-rind development. *Catena* **58**, 65–75.
- Pelt E., Chabaux F., Innocent C., Navarre-Sitchler A. K., Sak P. B. and Brantley S. L. (2008) Uranium-thorium chronometry of weathering rinds: rock alteration rate and paleo-isotopic record of weathering fluids. *Earth Planet. Sci. Lett.* **276**, 98–105.
- Plater A. J., Ivanovich M. and Dugdale R. E. (1992) Uranium series disequilibrium in river sediments and waters: the significance of anomalous activity ratios. *Appl. Geochem.* **7**, 101–110.
- Pogge von Strandmann P. A. E., Burton K. W., Porcelli D., James R. H., van Calsteren P. and Gislason S. R. (2011) Transport and exchange of U-series nuclides between suspended material, dissolved load and colloids in rivers draining basaltic terrains. *Earth Planet. Sci. Lett.* **301**, 125–136.
- Porter S. C. (1975) Weathering rinds as a relative-age criterion: application to subdivision of glacial deposits in the Cascade Range. *Geology* **3**, 101–104.
- Rad S., Louvat P., Gorge C., Gaillardet J. and Allegre C. J. (2006) River dissolved and solid loads in the Lesser Antilles: new insight into basalt weathering processes. *J. Geochem. Explor.* **88**, 308–312.
- Rasmussen C., Brantley S., Richter D., Blum A., Dixon J. and White A. F. (2011) Strong climate and tectonic control on plagioclase weathering in granitic terrain. *Earth Planet. Sci. Lett.* **301**, 521–530.
- Riebe C. S., Kirchner J. W. and Finkel R. C. (2004) Erosional and climatic effects on long-term chemical weathering rates in granitic landscapes spanning diverse climate regimes. *Earth Planet. Sci. Lett.* **224**, 547–562.
- Rosholt J., Doe B. and Tatsumoto M. (1966) Evolution of the isotopic composition of uranium and thorium in soil profiles. *Geol. Soc. Am. Bull.* **77**, 987–1004.
- Sak P. B., Fisher D. M., Gardner T. W., Murphy K. and Brantley S. L. (2004) Rates of weathering rind formation on Costa Rican basalt. *Geochim. Cosmochim. Acta* **68**, 1453–1472.
- Sak P. B., Navarre-Sitchler A. K., Miller C. E., Daniel C. C., Gaillardet J., Buss H. L., Lebedeva M. I. and Brantley S. L. (2010) Controls on rind thickness on basaltic andesite clasts weathering in Guadeloupe. *Chem. Geol.* **276**, 129–143.
- Samper A., Quidelleur X., Lahitte P. and Mollex D. (2007) Timing of effusive volcanism and collapse events within an oceanic arc island: Basse-Terre, Guadeloupe archipelago (Lesser Antilles Arc). *Earth Planet. Sci. Lett.* **258**, 175–191.
- Sarin M. M., Krishnaswami S., Somayajulu B. L. K. and Moore W. S. (1990) Chemistry of uranium, thorium, and radium isotopes in the Ganga-Brahmaputra river system – weathering processes and fluxes to the Bay of Bengal. *Geochim. Cosmochim. Acta* **54**, 1387–1396.
- Shirvington P. J. (1983) Fixation of radionuclides in the 238U decay series in the vicinity of mineralized zones: 1. The Austatom Uranium Prospect, Northern Territory, Australia. *Geochim. Cosmochim. Acta* **47**, 403–412.
- Sims K. W. W., Gill J. B., Dosseto A., Hoffmann D. L., Lundstrom C. C., Williams R. W., Ball L., Tollstrup D., Turner S., Prytulak J., Glessner J. G., Standish J. J. and Elliott T. (2008) An inter-laboratory assessment of the thorium isotopic composition of synthetic and rock reference materials. *Geostand. Geoanal. Res.* **32**, 65–91.
- Vigier N., Bourdon B., Turner S. and Allegre C. J. (2001) Erosion timescales derived from U-decay series measurements in rivers. *Earth Planet. Sci. Lett.* **193**, 485–499.
- Walker J., Hays P. and Kasting J. (1981) A negative feedback mechanism for the long-term stabilization of Earth's surface temperature. *J. Geophys. Res.* **86**, 9776–9782.
- West A. J., Galy A. and Bickle M. (2005) Tectonic and climatic controls on silicate weathering. *Earth Planet. Sci. Lett.* **235**, 211–238.
- White A. F., Blum A. E., Schulz M. S., Vivit D. V., Stonestrom D. A., Larsen M., Murphy S. F. and Eberl D. (1998) Chemical weathering in a tropical watershed, Luquillo Mountains, Puerto Rico: I. Long-term versus short-term weathering fluxes. *Geochim. Cosmochim. Acta* **62**, 209–226.
- Wolff-Boenisch D., Gislason S. r., Oelkers E. H. and Putnis C. V. (2004) The dissolution rates of natural glasses as a function of their composition at pH 4 and 10.6, and temperatures from 25 to 74 degree C. *Geochim. Cosmochim. Acta* **68**, 4843–4858.